

**SIMULATION OF AN ROC-BASED THERMAL ENERGY STORAGE SYSTEM IN CHARGE
 AND DISCHARGE CYCLES**

**Rozina N. Nalbandian, Karen U. Girgis, Benjamin T. Kong, Ulyses Aguirre, Adrian Gil C. Victorio,
 Justin Andrew Lee, and Reza Baghaei Lakeh***

Mechanical Engineering Department
 California State Polytechnic University, Pomona
 Pomona, California, USA

ABSTRACT

In this paper, Computational Fluid Dynamics (CFD) is employed to investigate the heat transfer characteristics of Reverse Osmosis Concentrate (ROC) as an alternative, low-cost thermal energy storage medium. Thermal energy storage is a critical component for increasing efficiency and dispatchability of solar thermal and combined heat and power plants. The by-product of water desalination, ROC, is classified as an industrial waste by the U.S. Environmental Protection Agency as it has negative effects on vegetation and sea-life. Currently, ROC disposal includes deep-well injection, surface discharge to rivers, discharge to the ocean, and evaporation ponds. The composition and thermal properties of ROC salt vary depending on the original source of feedwater. Transient models are utilized to understand the heat transfer between the heat transfer fluid and storage fluid (i.e., ROC) over time. This simulation also provides valuable information in determining the optimal operating conditions of the thermal energy storage system. This information will be used in conjunction with a cost analysis, focused on the transportation, processing and containment cost of the energy storage, that aims to determine the economic feasibility of ROC technology in large scale, commercial applications.

Keywords: Renewable Energy, Thermal Energy Storage

NOMENCLATURE

| | |
|-----------------------|--|
| A | Area of the surface exposed to environment |
| E | Energy |
| E_{stored} | Total energy stored in the device |
| G_b | Turbulence generation (buoyancy) |
| G_k | Turbulence generation (mean velocity gradient) |
| $H_{in,air}$ | Enthalpy of air going in |
| $H_{out,air}$ | Enthalpy of air going out |
| \vec{J}_j | Diffusion flux of species j |
| L | Characteristic length |
| $\overline{N_{uL,B}}$ | Nusselt number for the bottom side |
| $\overline{N_{uL,T}}$ | Nusselt number for the top side |

| | |
|-----------------------|--|
| $\overline{N_{uL,V}}$ | Nusselt number for the vertical side |
| PCM | Phase change material |
| Pr | Prandtl number for air |
| Q | Volumetric flow rate of air |
| Ra_L | Rayleigh number |
| Re | Reynolds Number |
| ROC | Reverse Osmosis Concentrate |
| S_h | Source term |
| T_{film} | Film Temperature (°C) |
| $T_{in,air}$ | Inlet temperature of air |
| $T_{out,air}(t)$ | Outlet temperature of air as a function of time |
| T_s | Surface temperature (°C) |
| $T_s(t)$ | Surface temperature as a function of time |
| T_∞ | Ambient environment air temperature (°C) |
| T^* | Threshold Temperature |
| Y_m | Fluctuating dilation in compressible turbulence |
| $c_{p,air}$ | Specific heat of air |
| d | derivative of |
| \underline{g} | Gravity (m/s ²) |
| \bar{h} | Average heat convection coefficient |
| h_j | Sensible Enthalpy |
| k_{air} | Thermal conductivity of air |
| k_t | Turbulence kinetic energy |
| \dot{m} | Mass flow of air |
| p | pressure |
| q | Heat rate due to convection |
| q_{loss} | Heat rate loss during charging or discharging |
| \vec{v} | Velocity |
| α | Thermal diffusivity of air |
| β | Thermodynamic Beta for ideal gas, air (K ⁻¹) |
| ε | Turbulence dissipation rate |
| ν | Kinematic viscosity of air |
| ρ | Density |
| σ_k | Turbulence Prandtl number for k_t |
| σ_ε | Turbulence Prandtl number for ε |
| $\bar{\tau}$ | Stress tensor |
| μ | Dynamic viscosity |
| μ_t | Eddy viscosity |

1. INTRODUCTION

Due to the increase of human induced climate change in the last decade, governments have been focusing more on utilizing renewable energy sources, such as solar, wind, and hydro. Solar energy, in particular, has many advantages such as being a clean, affordable, and widely distributable alternative compared with other renewable energy sources. However, the widespread application of solar energy is limited by its intermittent availability [1]. Thermal Energy Storage (TES) is one of the methods of storing excess solar thermal power and then delivering that power back to the grid when demand outpaces availability of solar energy. Phase Change Materials (PCM), are particularly of interest as TES mediums due to their high energy storage density [2].

Inorganic salts as a PCM are well-suited to address both the higher operating temperature needs of solar power towers and the attendant need for TES, as they can be used as a thermal storage media in advanced high temperature concentrating solar power plants (CSP) [3]. The use of Reverse Osmosis Concentrate (ROC) as a high temperature TES medium allows for higher efficiency of steam power generation, in comparison to the use of Solar Salts (NaNO₃/KNO₃). Typical solar salt with a 60/40 weight ratio of NaNO₃ and KNO₃ melts at 220°C and is stored at 565°C [4], whereas the ROC being researched melts between roughly 450°C and 638°C. Widespread use of ROC-based TES has the potential to prevent further environmental harm caused by the discharge of concentrated salt and chemicals that may pose adverse effects on the coastal marine ecosystem [5].

The team aims to study how to use ROC in traditional TES systems that can be charged by direct solar thermal or electric resistive heating. In order to characterize the heat transfer during the charging and discharging cycles, Computational Fluid Dynamics (CFD) was employed. The main goal of this study is simulating an existing heat storage system that uses ROC salt as a storage medium. The focus is on thermal interactions between the heat transfer fluid and storage fluid during charging and discharging. Figure 1 shows a schematic of developing an ROC-based TES system for solar-thermal and grid-scale applications.

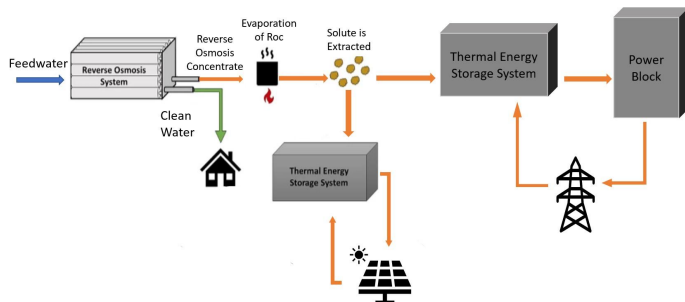


FIGURE 1: Development of a Thermal Energy Storage using ROC

2. MATERIALS AND METHODS

A simplified model of an existing experimental setup was created and imported into ANSYS. Figure 2 shows a

summary of some of the boundary conditions and Table 1 is a summary of material properties used for the simulations.

The ANSYS model includes one square tube element containing ROC, the tube element's shell, baffles, and air flow domain as shown in Fig. 3. The boundary conditions and assumptions of the simulation are as follows. The inlet velocity is 4.769 m/s, based on the properties of the available air blower, and the outlet is at ambient pressure. Ambient pressures and temperatures are used for air outside the system. Natural convection is considered for all external boundaries to quantify the losses. For discharge, the air flowing in from the inlet is at ambient temperature while the system is initially set to a higher temperature, and vice versa for charging. There is a no slip condition on all of the walls. The salt's thermal properties are based on NaCl and salt shell material is made of steel. Lastly, as the system is symmetrical, one side of the symmetry was simulated assuming symmetry boundary condition.

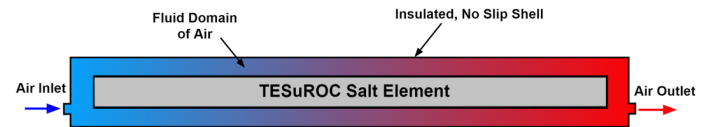


FIGURE 2: Flow Diagram

TABLE 1: Summary of Properties Used for the Materials of Air, Steel, Salt, and Insulation

| Property: \ Material: | Density (kg/m ³) | Specific Heat (J/kg-K) | Thermal Conductivity (W/m-K) | Viscosity (kg/m-s) |
|-----------------------|------------------------------|------------------------|------------------------------|--------------------|
| Air | 1.225 | 1006.43 | 0.0242 | 1.7894e-05 |
| Steel | 8030 | 502.48 | 16.27 | - |
| ROC (Solid) | 2170 | 975.359 | 4.85 | - |
| Insulation | 128.148 | 0.284 | 0.0625 | - |

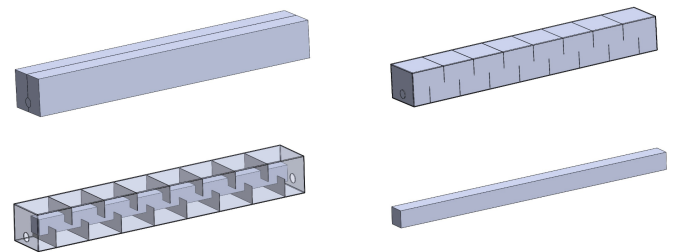


FIGURE 3: Outer Shell (Top Left), Flow Domain (Top Right), Shell and Baffles (Bottom Left), and Salt Element (Bottom Right) Right

A 3D mesh was generated on the geometry as shown in Fig. 4. Elements are made finer and clustered in regions where a larger gradient of variables is expected. The mesh used for the

simulations in the paper was designed to focus on critical areas of the system. The four corners, inlet and outlet regions, and regions around the baffles contained smaller element sizes. The finalized mesh contains a total of 2.91 million elements and 700 thousand nodes. The convergence criteria were set to 1e-04 for momentum and continuity equation and 1e-06 for energy equation.

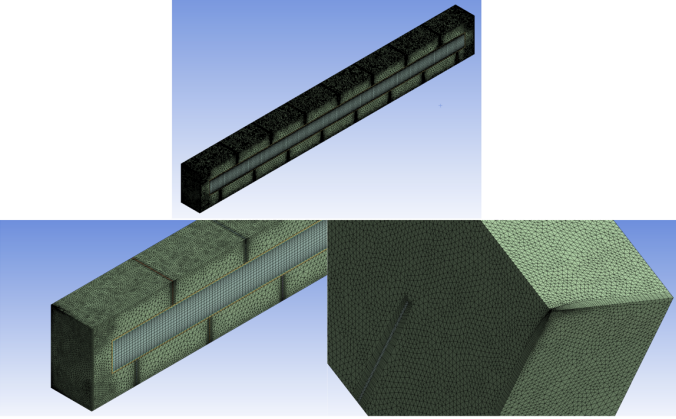


FIGURE 4: Computational Grid

The solution was obtained adopting the following steps. First, the solver was set up only to calculate the momentum and equations in steady state. A pressure-based solver was used with absolute velocity formulation and steady time [6]. The air flow rate of the inlet was set to mirror the effects of the air blower used in the lab. Afterwards, with the steady state solution preserved, the flow equation was turned off and the energy equation was turned on to extract temperature changes during discharge. Therefore, solver settings were changed to transient and the calculation was run until the average salt element temperature reached was low enough such that the discharge threshold temperature, T^* , equaled 0.1. This was done under the assumption that flow is constant even as the temperature of the system changes.

$$T^* = \frac{T_{avg} - T_{inlet}}{T_{initial} - T_{inlet}} = 0.1 \quad (1)$$

The governing equations of the problem are continuity, momentum and energy conservation as given in Eqs. (2-4). The steady state values, such as pressure and velocity, were obtained by utilizing these governing equations in Ansys. Ansys utilizes differential elements based on the number of nodes created by the mesh to calculate values. [6]

$$\frac{\partial}{\partial t}(\rho) + \nabla \cdot (\rho \vec{v}) = 0 \quad (2)$$

$$\frac{\partial}{\partial t}(\rho \vec{v}) + \nabla \cdot (\rho \vec{v} \vec{v}) = -\nabla p + \nabla \cdot (\underline{\tau}) + \rho \vec{g} + \vec{F} \quad (3)$$

$$\frac{\partial}{\partial t}(\rho E) + \nabla \cdot [\vec{v}(\rho E + p)] = \nabla \cdot [\nabla T - \sum_j h_j \vec{J}_j] + (\bar{\tau} + \vec{v}) \quad (4)$$

The heat transfer fluid is air and was modeled as turbulent flow. This turbulent flow was solved using the standard k- ϵ model. This model is valid when modeling fluid that has uniform turbulent properties. The governing equation for simulating turbulent kinetic energy and dissipation are given in Eqs. (5-6). [6]

$$\begin{aligned} \frac{\partial}{\partial t}(\rho k_t) + \frac{\partial}{\partial x_i}(\rho k_t u_i) \\ = \frac{\partial}{\partial x_j} \left[\left(\mu + \frac{\mu_t}{\sigma_k} \right) \frac{\partial k_t}{\partial x_j} \right] + G_k + G_b - \rho \epsilon - Y_M \end{aligned} \quad (5)$$

$$\begin{aligned} \frac{\partial}{\partial t}(\rho \epsilon) + \frac{\partial}{\partial x_i}(\rho \epsilon u_i) \\ = \frac{\partial}{\partial x_j} \left[\left(\mu + \frac{\mu_t}{\sigma_\epsilon} \right) \frac{\partial \epsilon}{\partial x_j} \right] + C_{1\epsilon} \frac{\epsilon}{k_t} (G_k + C_{3\epsilon} G_b) - C_{2\epsilon} \rho \frac{\epsilon^2}{k_t} \end{aligned} \quad (6)$$

The eddy viscosity term, μ_t , in Eq.(7) is defined as

$$\mu_t = \rho C_\mu \frac{k_t^2}{\epsilon} \quad (7)$$

In the standard k- ϵ model, the empirical constants were $C_{1\epsilon} = 1.44$, $C_{2\epsilon} = 1.92$, $C_\mu = 0.09$, $\sigma_k = 1.0$, $\sigma_\epsilon = 1.3$ based off of experiments for fundamental turbulent flow. With these equations, Ansys can solve for an accurate approximation of velocity and pressure. [6]

The transient simulations for discharge temperature modeling were calculated with a system initial temperature of 500 °C, 600 °C, 800 °C, and 1000 °C and ambient air entering the inlet at 22°C. To accurately characterize convection heat loss between the system and the ambient air, natural convection heat transfer calculations were done on the exterior surfaces of the heat storage element. Raleigh number for the respective sides of the shell [7],

$$Ra_L = \frac{g\beta(T_s - T_\infty)L^3}{\nu\alpha} \quad (8)$$

The Raleigh number is used to obtain natural convection coefficients on all sides. Since the left and right side of the shell are vertically oriented, they will be treated as vertical plates. The Nusselt number for the left and right vertical plates is [7]:

$$\overline{Nu_{L,V}} = \left(0.825 + \frac{0.387 Ra_L^{\frac{1}{4}}}{[1 + (0.492 Pr)^{\frac{1}{4}}]^{2/7}} \right)^2 \quad (9)$$

Since the top and bottom side of the shell are flat and horizontally oriented, they will be treated as horizontal plates. The top and bottom side has different Nusselt numbers since the top side has a hot surface facing upwards and the bottom side has the hot surface facing downward. The Nusselt number for the top side (hot surface facing upward) is,

$$\overline{Nu}_{L,T} = 0.54 Ra_L^{\frac{1}{4}} \quad (10)$$

for Raleigh number in the range of $10^4 < Ra_L < 10^7$ for Raleigh number in the range of $(10^7 < Ra_L < 10^{11})$

The Nusselt number for the bottom side (hot surface facing downward) is,

$$\overline{Nu}_{L,B} = 0.52 Ra_L^{\frac{1}{5}} \quad (11)$$

for Raleigh number in between $10^4 < Ra_L < 10^9$

Using the calculated Nusselt number, the average heat transfer convection coefficient can be found for the respective sides.

$$\bar{h} = \frac{\overline{Nu}k_{air}}{L} \quad (12)$$

Using the heat convection coefficient, the total heat rate loss is based on Newton's Second Law of Cooling [7]:

$$q = \bar{h} A(T_s - T_\infty) \quad (13)$$

Energy balance on a control volume around the thermal energy storage is used to quantify the energy storage capacity using Eq. (14)

$$T_{in,air}(\rho Q c_{p,air} + hA)\Delta t - \rho Q c_{p,air} \int T_{out,air}(t)dt - hA \int T_s(t)dt = E_{stored} \quad (14)$$

3. RESULTS AND DISCUSSION

3.1 Discharge Cycle

In the discharge simulation, the temperature for T^* was calculated for the four cases of maximum temperature at 500°C, 600°C, 800°C, and 1000°C as listed in Table 2. The assembly was initialized at a maximum temperature for each case and the air flowing from the inlet was set to 22°C, mimicking the air blower temperature used in the physical setup during the discharge phase. During the ANSYS simulation, the salt was cooled while remaining as a solid.

TABLE 2: Simulated Discharge Cycle Time Estimates

| T_{Max} (°C) | 500 | 600 | 800 | 1000 |
|----------------|-------|-------|-------|--------|
| T_{End} (°C) | 61.07 | 79.47 | 99.31 | 119.80 |
| Time (s) | 4905 | 4580 | 4460 | 4641 |

To validate the results of the ANSYS simulation, a mesh refinement was conducted to compare steady state calculation results to results calculated with varying meshes. In this mesh refinement, two coarser meshes were generated so that the number of elements was roughly one third and one ninth the number of elements in the original mesh. All three meshes are shown in Fig. 5.

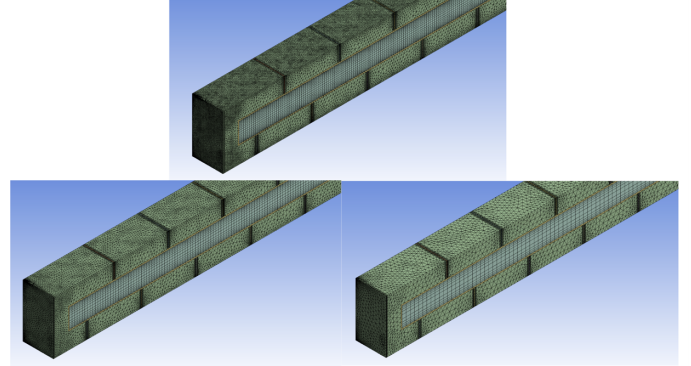


FIGURE 5: Mesh Refinement

To compare the steady state results of the original mesh and two coarser meshes, pressure and velocity data were extracted along a straight line plotted along the side of the system as seen in Fig. 6. Figures 7 and 8 show the mesh refinement study results. Although there were some large inconsistencies for the velocity data at the inlet, it can be assumed that the discrepancies were mainly due to the initial backflow. Overall, the other sections of the mesh can be seen to have overlapping data.

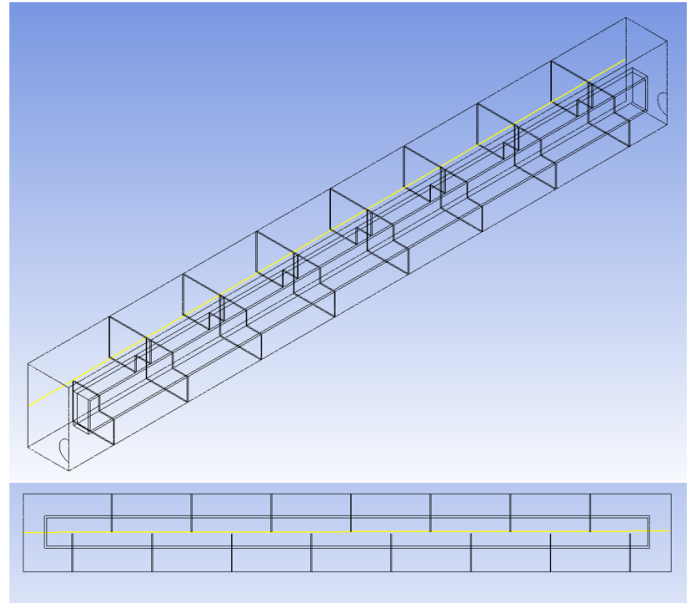


FIGURE 6: Line of Data Extraction

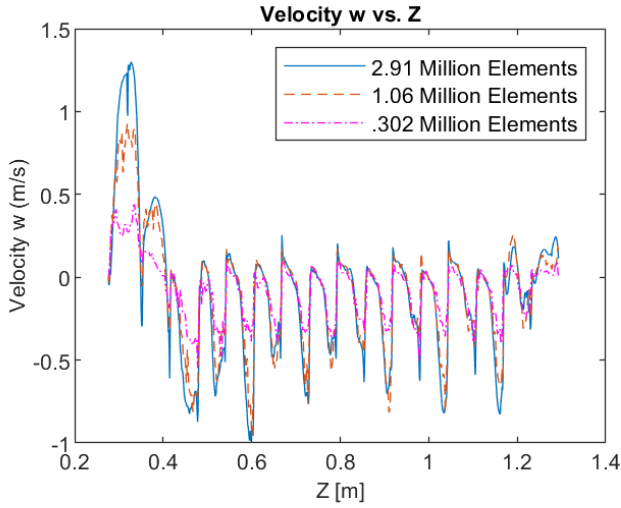


FIGURE 7: Velocity, w versus Length (Z-Direction)

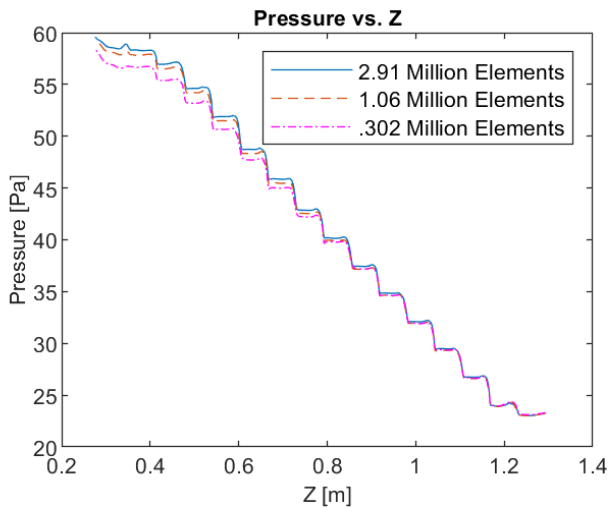


FIGURE 8: Pressure versus Length, (Z-Direction)

Figure 9 shows the heat transfer flow streamlines superimposed on the pressure contour plots. The baffles complicate the flow path and increase the residence time of the air in the TES module. The discharge time was calculated for all cases

At the inlet, a velocity was assigned of 4.769 m/s in the z-direction. The velocity is at a maximum as it enters the model, but then quickly drops as the flow hits the baffles. The inlet was also assigned to have a turbulent intensity of 5% and a hydraulic diameter of 1.25 in (0.03175 m). After the fluid velocity settles from the eddy created at the entrance, an alternating pattern can be seen from 0.4 m to 1.2 m due to the baffle spacing.

As shown in Fig. 9, maximum pressure is at the inlet, and it decreases as flow moves towards the outlet. The pressure drops are correlated to the specifications of the configuration. Baffle spacing and the number of baffles cause a greater amount

of heat transfer and pressure drop. Also based on tests conducted between three different sets of baffles, the model with more baffles showed to have a smaller recirculation zone [9].

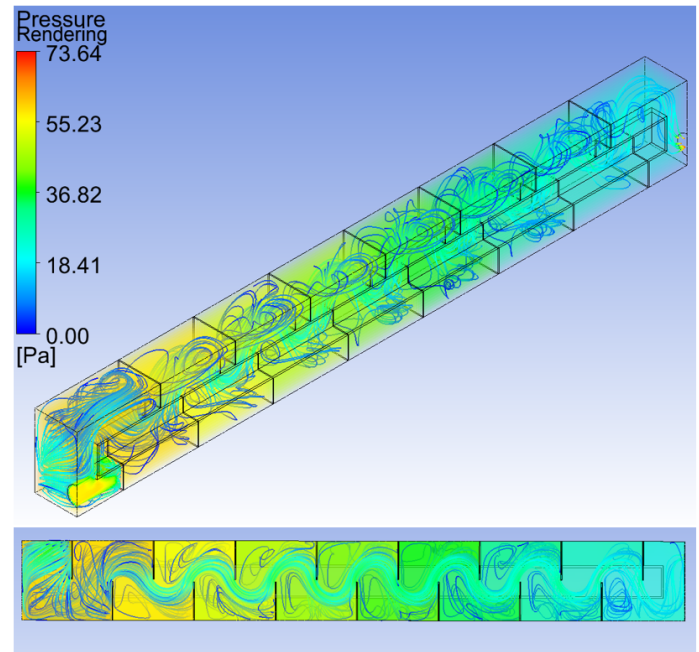


FIGURE 9: Pressure Render with Velocity Streamlines

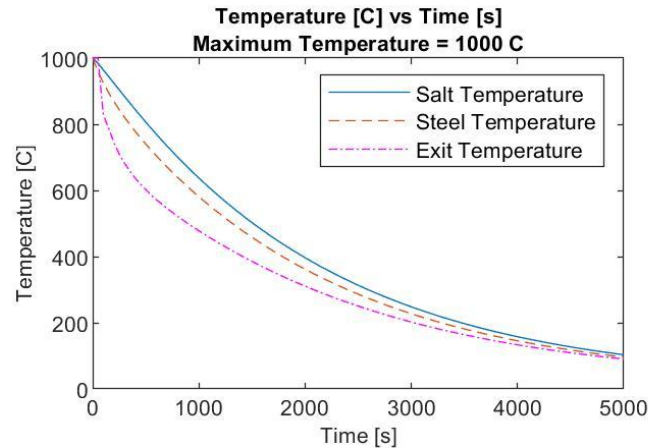


FIGURE 10: Temperature vs Time of Salt, Outlet and Steel for the Discharge Cycle with a Maximum Temperature of 1000 °C

Figure 10 displays a plot of the temperature of the salt, steel (consisting of the baffles and the salt shell), and the exit temperatures as the system is cooled for 5000 seconds of flow time [10]. The behavior of the discharge phase of Fig. 10 is similar to the results in Niyas [11]. It is notable from Figure 11 that the salt element stores the heat and provides the heat for the heat transfer fluid (air) during discharge.

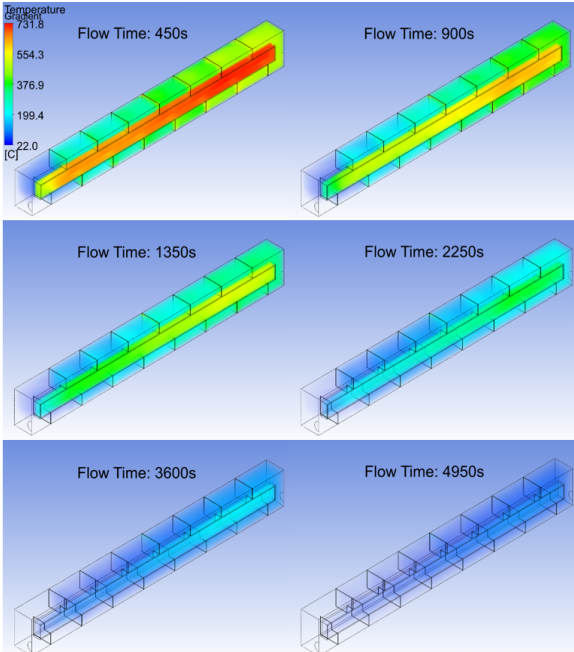


FIGURE 11: Temperature Gradient Contour Plots for Discharge Cycle Initialized at 800°C

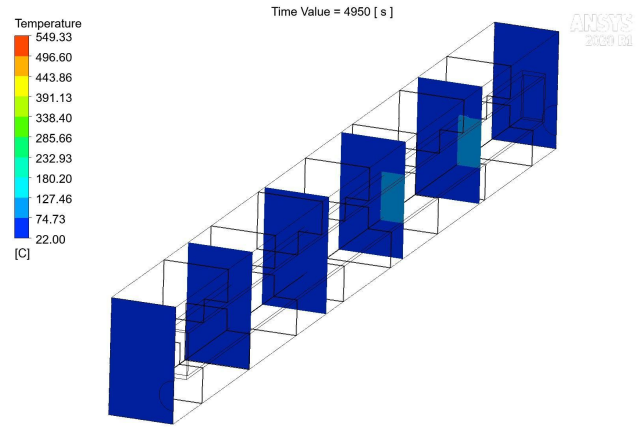


FIGURE 12: Discharge Starting at 600°C

Figure 12 illustrates the temperature contour plots on 6 cross sections of the model. The mixing caused by the turbulent heat transfer fluid provides a nearly uniform temperature on the cross section of the module. There is a significant longitudinal gradient in the salt element due to extraction of thermal energy along the module.

3.2 Charge Cycle

The simulation was initialized at 22°C and element was charged with the inlet set at the maximum temperature for each case. This method would mimic the air blower temperature used in the physical setup during the charge phase. The charge time was calculated for the four cases of maximum temperature at 500°C, 600°C, 800°C, and 1000°C as listed in Table 3.

TABLE 3: Simulated Charge Cycle Time Estimates

| T _{Max} (°C) | 500 | 600 | 800 | 1000 |
|-----------------------|--------|--------|--------|--------|
| T _{End} (°C) | 452.2 | 542.2 | 722.2 | 902.2 |
| Time (s) | 6363.4 | 6554.1 | 6532.7 | 6525.7 |

The charge cycle simulation for each case was run under transient settings until the average salt element temperature reached the end temperature listed in Table 3. At this end temperature, the charge threshold temperature, T*, would be equal to 0.9. This threshold temperature is shown below in Eq.(15). Comparing the estimated results from Table 2 and Table 3, it is evident that the discharge cycle takes a longer time compared to the charge cycle, for its threshold temperature to reach its designated value of 0.1 and 0.9, respectively,

$$T^* = \frac{T_{avg} - T_{initial}}{T_{inlet} - T_{initial}} = 0.9 \quad (15)$$

By simulating the charge cycle for each case until T* reaches its threshold value of 0.9 (90% charged), the estimated charge times were found and listed in Table 3.

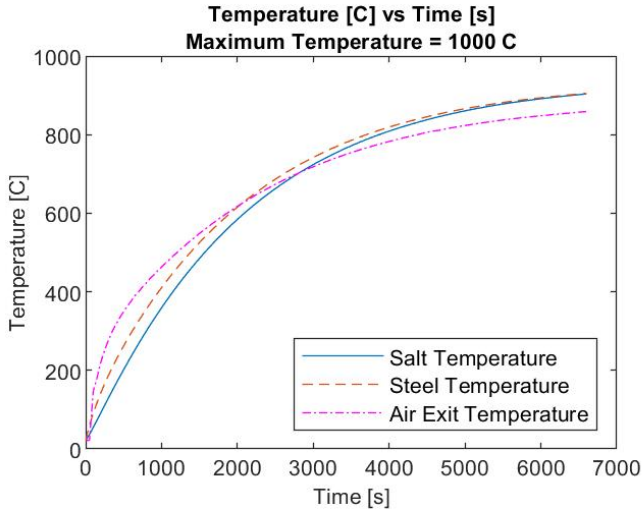


FIGURE 13: Temperature vs Time of Salt, Outlet and Steel for Charge Cycle

Figure 13 displays a plot of the temperature of the salt, steel (consisting of the baffles and the salt shell), and the exit temperatures for the case of a maximum temperature of 1000°C. The behavior of the charge phase of Fig. 13 is similar to the results in Niyas [11]. It is notable that after a certain time, the salt has the highest temperature in the charging process.

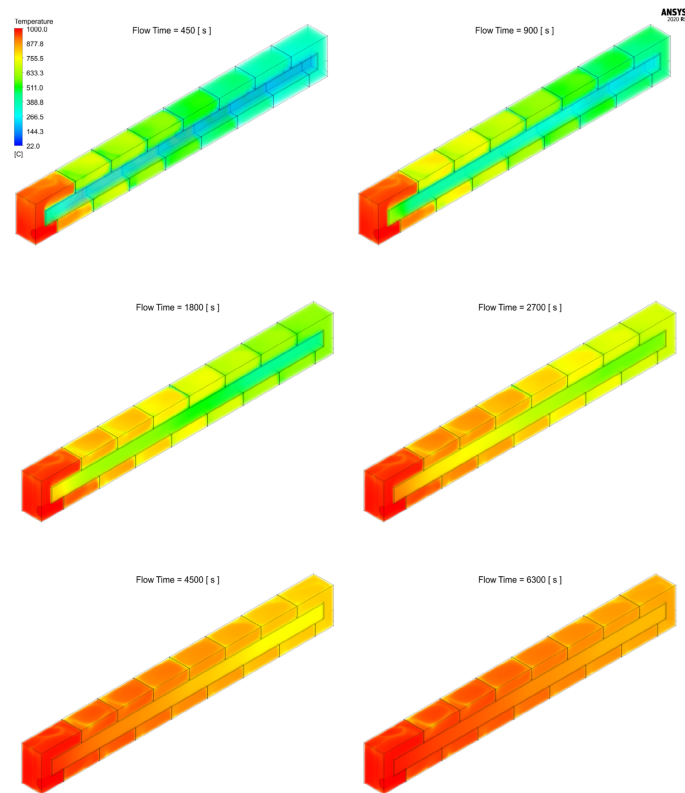


FIGURE 14: Temperature Gradient Contour Plots for Charge Cycle for the 1000°C Case

Figure 14 displays the TES as it is being thermally charged over time. The salt element is charged in an unsteady fashion showing a front of high temperature region in the salt element to move from inlet towards exit, as expected.

Contour plots of six equidistant planes can be viewed in Fig. 15 for the 1000°C case at 450 seconds, 2700 seconds, and 6300 seconds of flow time. These contour plots provide a more detailed description of the temperature behavior at different locations throughout the TES. Similar to Fig. 14, the overall temperature of each plane becomes warmer the closer the plane is towards the inlet side of the TES. This figure also provides a look into the behavior of the salt element at different points along the length of the TES.

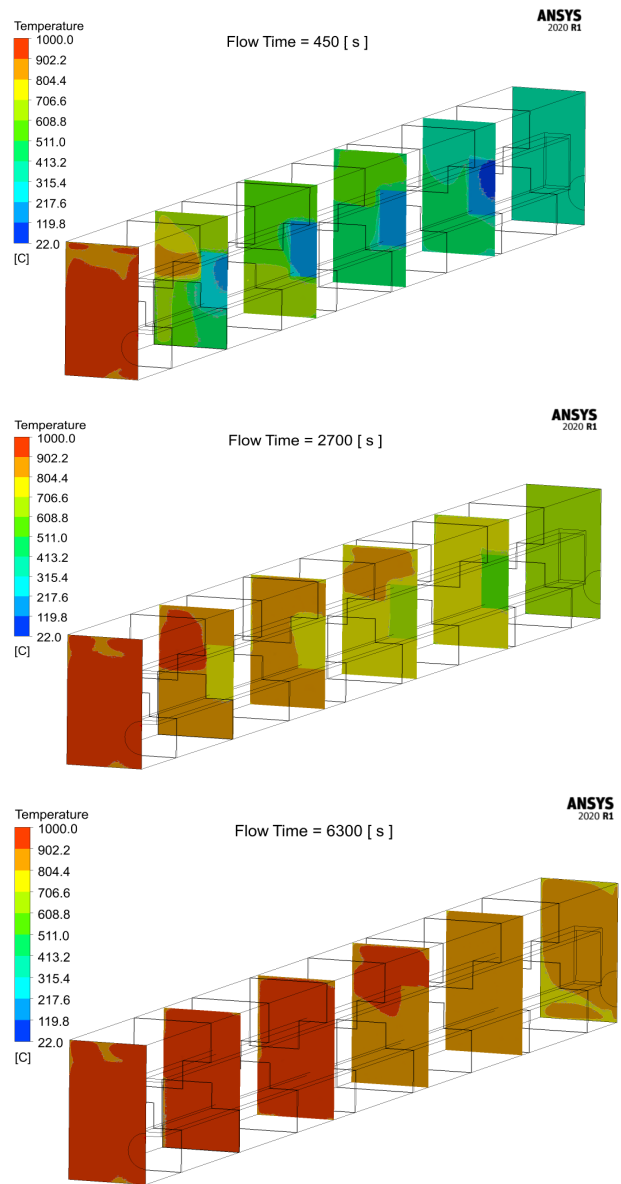


FIGURE 15: Charge Starting for 1000°C Case

4. CONCLUSION

The charging and discharging cycles of an ROC-based thermal energy storage module was simulated computationally. The computational results are verified by a grid refinement study. The results show that there is sufficient energy extracted during the discharge phase to create hot air at a temperature suited for power generation.

Both charge and discharge cycles create significant longitudinal temperature gradients inside the salt element. The mixing of the heat transfer fluid is caused by the baffles and provides a nearly uniform temperature on the cross section of the module.

The results show that the charge time will be more time than discharge time due to thermal conductivity limitations of the ROC salt.

ACKNOWLEDGEMENTS

This work was supported by grant No. R18AC00087 and No. R19AC00090 from United States Department of Interior, Bureau of Reclamation. The authors would like to thank ANSYS Inc. for providing COVID licenses.

REFERENCES

- [1] Navarrete, Nuria, Mondragón, Rosa, Wen, Dongsheng, Navarro, Maria Elena, Ding, Yulong, and Juliá, J. Enrique. "Thermal Energy Storage of Molten Salt –based Nanofluid Containing Nano-encapsulated Metal Alloy Phase Change Materials." *Energy (Oxford)* 167 (2019): 912-20. Web.
- [2] Zhang, P, Xiao, X, Meng, Z.N, and Li, M. "Heat Transfer Characteristics of a Molten-salt Thermal Energy Storage Unit with and without Heat Transfer Enhancement." *Applied Energy* 137 (2015): 758-72. Web.
- [3] Zhang, P, Ma, F, and Xiao, X. "Thermal Energy Storage and Retrieval Characteristics of a Molten-salt Latent Heat Thermal Energy Storage System." *Applied Energy* 173 (2016): 255-71. Web.
- [4] Kearney, D, B Kelly, R Cable, N Potrovitza, U Herrmann, P Nava, R Mahoney, J Pacheco, D Blake, and H Price. "Overview on Use of a Molten Salt HTF in a Trough Solar Field." *NREL TES Workshop-Golden_Feb03* NREL/PR-550-40028 (February 20, 2003). <https://www.nrel.gov/docs/fy03osti/40028.pdf>.
- [5] Palomar, P., & J., I. (2011). Impacts of Brine Discharge on the Marine Environment. Modelling as a Predictive Tool. *Desalination, Trends and Technologies*. doi:10.5772/14880
- [6] ANSYS Fluent Theory Guide (16.1 ed.). (2015). ANSYS, Inc.
- [7] *Fundamentals of Heat and Mass Transfer*. Place of Publication Not Identified: John Wiley, 2016. Print.
- [8] Kenisarin, Murat M. "High-temperature Phase Change Materials for Thermal Energy Storage." *Renewable & Sustainable Energy Reviews* 14.3 (2010): 955-70. Web.
- [9] Sadikin, A & Khian, N & Hwey, Y & Al-Mahdi, H & Taib, Ishkrizat & Sadikin, A & Md, S & Ayop, Sallehuddin & Akademia Baru, Penerbit. (2018). Effect of Number of Baffles on Flow and Pressure Drop in a Shell Side of a Shell and Tube Heat Exchangers. 156-164.
- [10] N, Beemkumar & Karthikeyan, Alagu & Reddy, Kota & Rajesh, Kona & Arul, Anderson. (2017). Analysis of Thermal Energy Storage Tank by ANSYS and Comparison with Experimental Results to Improve its Thermal Efficiency. IOP Conference Series: Materials Science and Engineering. 197. 012039. 10.1088/1757-899X/197/1/012039.
- [11] Niyas, H., Prasad, S., & Muthukumar, P. (2017). Performance investigation of a lab-scale latent heat storage prototype – Numerical results. *Energy Conversion and Management*, 135, 188-199. doi:10.1016/j.enconman.2016.12.075